Seeds of locally aligned motion and stress coordinate collective cell migration - Supporting information

Assaf Zaritsky,[1,2,*] Erik S. Welf,[1,2] Yun-Yu Tseng,[3] M Angeles Rabadán,[3] Xavier Serra-Picamal,[4] Xavier Trepat,[4] and Gaudenz Danuser[1,2,*]

[1]Department of Cell Biology, UT Southwestern Medical Center, Dallas, TX 75390, USA.

[2]Department of Bioinformatics, UT Southwestern Medical Center, Dallas, TX 75390, USA.

[3]Cell Biology Program, Memorial Sloan-Kettering Cancer Center, New York, NY 10065, USA.

[4]Institute for Bioengineering of Catalonia, ICREA, and University of Barcelona, Barcelona, Spain.

[*]Corresponding Authors: Gaudenz Danuser, E-mail: gaudenz.Danuser@utsouthwestern.edu; Assaf Zaritsky, E-mail: assafzar@gmail.com

- Supplementary figures
    - Supplementary Figure S1: Quantifying geometry index and plithotaxis index
    - Supplementary Figure S2: Estimated angular contribution of geometry and plithotaxis to the observed motion-stress alignment
    - Supplementary Figure S3: Spatial analysis of plithotaxis and geometry indices
    - Supplementary Figure S4: Spatiotemporal ratio between speed of cells inside and outside clusters
    - Supplementary Figure S5: Geometry index is enriched within coordinated motion clusters
    - Supplementary Figure S6: Depletion of several tight-junction proteins diminish motion-stress alignment by inhibiting translation of oriented stress to motion
    - Supplementary Figure S7: shear-strain events and flow patterns are temporally synchronized
    - Supplementary Figure S8: Shear-strain events guide multicellular flow patterns for HBEC wound healing experiments
    - Supplementary Figure S9: More examples of HBEC flow probabilities and shear-strain events
    - Supplementary Figure S10: More examples of HBEC accumulated flow probabilities and shear-strain events
    - Supplementary Figure S11: More examples showing that HBEC shear-strain events and flow patterns are temporally synchronized
    - Supplementary Figure S12: Detection of shear-strain events
- Supplementary Data S1: Assessing plithotaxis and geometry indices

- Supplementary Data S2: Spatial variation in plithotaxis
- Supplementary videos legends
    - Supplementary Video S1: Propagating motion-induced coordination in stress
    - Supplementary Video S2: Construction of protruding cells kymograph (HBEC)
    - Supplementary Video S3: HBEC wound healing time lapse phase contrast imaging

Supplementary figures

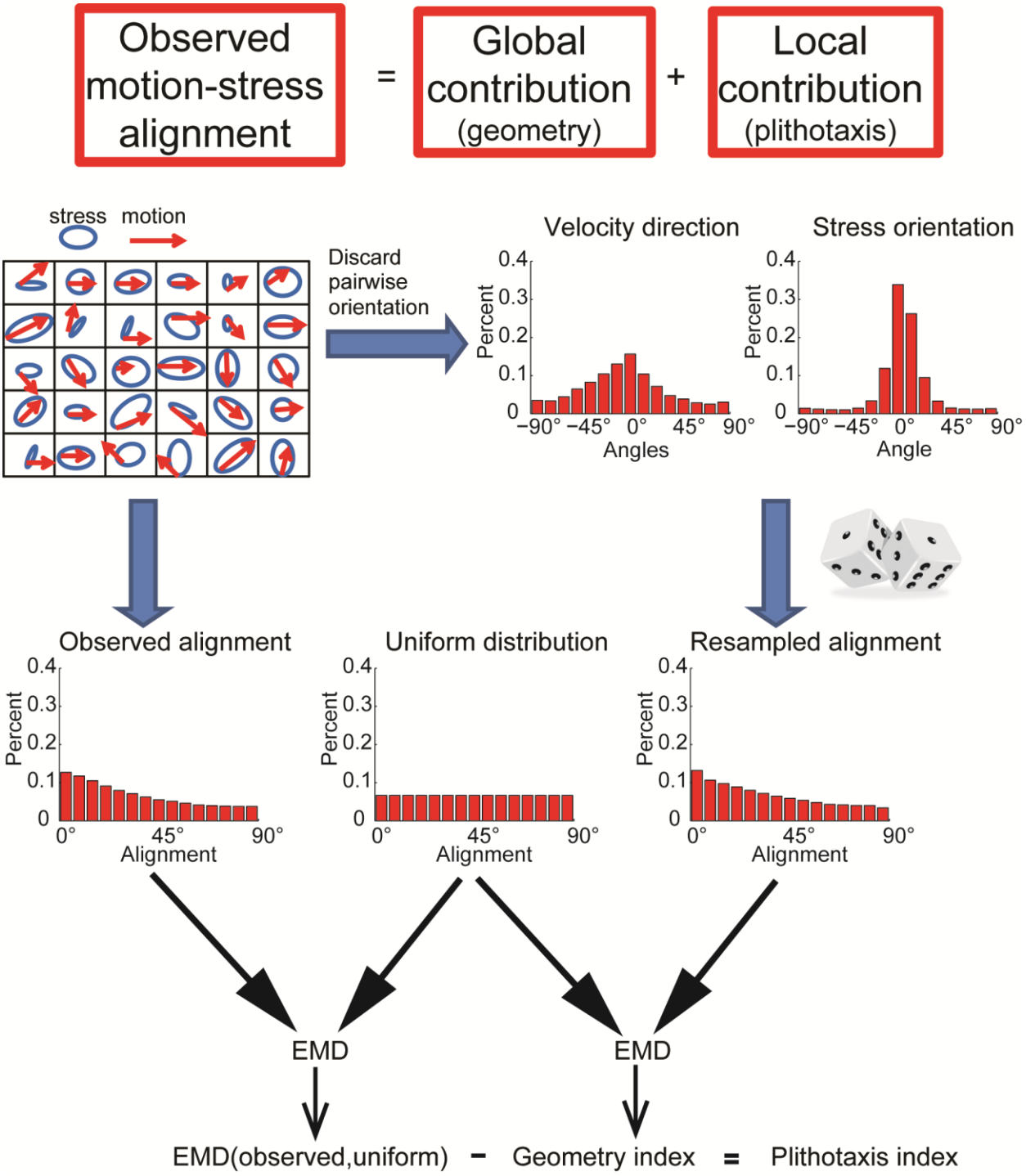

Figure S1: Quantifying geometry index and plithotaxis index. We assume that the observed motion-stress alignment can be modeled as the sum of two components: (1) global bias originating from physical constraints of the monolayer geometry, (2) local alignment of motion to stress orientation (plithotaxis). These components are separated by random and independent resampling from the corresponding marginal distributions of stress-orientation and velocity direction (resampled alignment). Earth movers distance (EMD), a measure of the distance between two probability distributions, is used to calculate the global bias (geometry index), as defined by the distance between uniform and resampled distributions. The plithotaxis index is calculated as the subtraction of the geometry index from the EMD between uniform and observed motion-stress alignment distributions (see Methods).

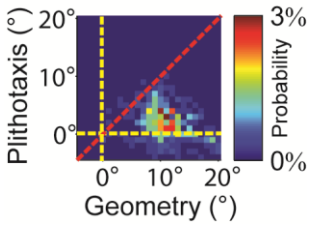

Figure S2: Estimated angular contribution of geometry and plithotaxis to the observed motion-stress alignment. Joint distribution of the estimated angular distribution of plithotaxis and geometry for all time points (n = 96) in all experiments (N = 4). The calculation was performed as follows. 45° is the expected mean alignment when no geometry or plithotaxis exist, corresponding to the scenario of a uniform distribution of velocity angles, stress orientations and no plithotaxis. The estimated contribution of plithotaxis to the observed motion-stress alignment is calculated as

$\theta_{plithotaxis} = (45° - \theta_{median}) \frac{plithotaxis\ index}{plithotaxis\ index + geometry\ index}$, and correspondingly

$\theta_{geometry} = (45° - \theta_{median}) \frac{geometry\ index}{plithotaxis\ index + geometry\ index}$. The left term corresponds to the difference between the observed and random alignment (high values correspond to better observed alignment), the right term corresponds to the relative contribution of plithotaxis (geometry) to the observed alignment. Median was used to reduce the effect of outliers.

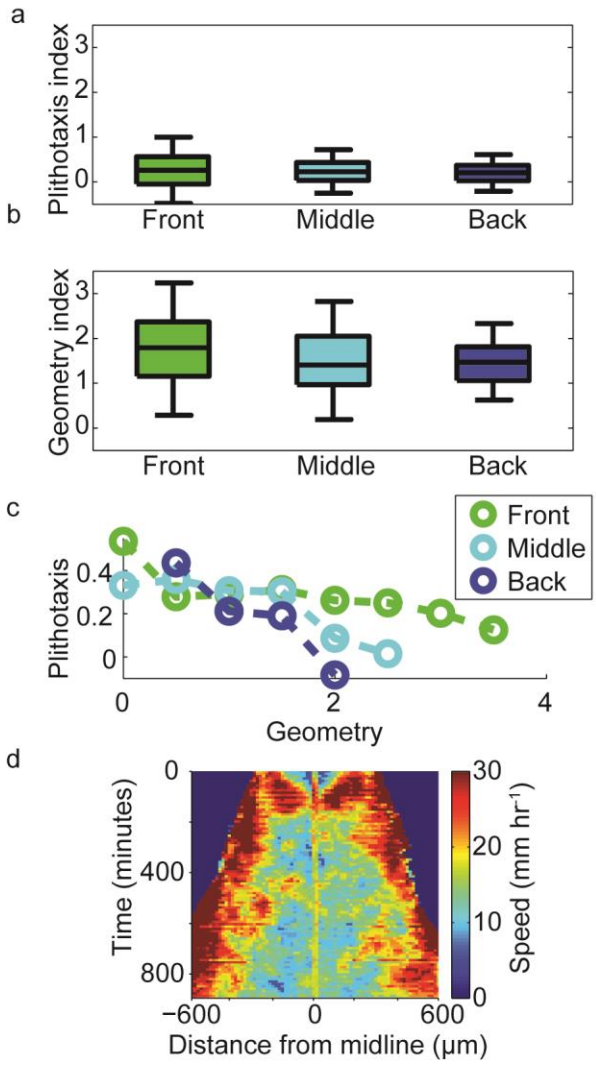

Figure S3: Spatial analysis of plithotaxis and geometry indices. (a-b) Three regions were defined for each time point, *front* (≤ 200 μm from monolayer edge), *middle* (≤ 400 μm) and *back* (≤ 600 μm). Plithotaxis and geometry index were calculated for each time point, the regions' width of 200 μm was selected to allow enough data for calculation of these indices. Data accumulated for all N = 4 independent experiments and n = 96 time points per experiment. (a) Plithotaxis index of front cells was ~1.2 fold higher compared to back cells (medians: front: 0.26, middle: 0.23, back: 0.20). (b) Geometry index of front cells was ~1.2 fold higher compared to back cells (medians: front: 1.79, middle: 1.41, back: 1.47). (c) Average plithotaxis index as a function of the geometry index. (d) Spatiotemporal kymograph demonstrating that fast cells are enriched close to the monolayer edge.

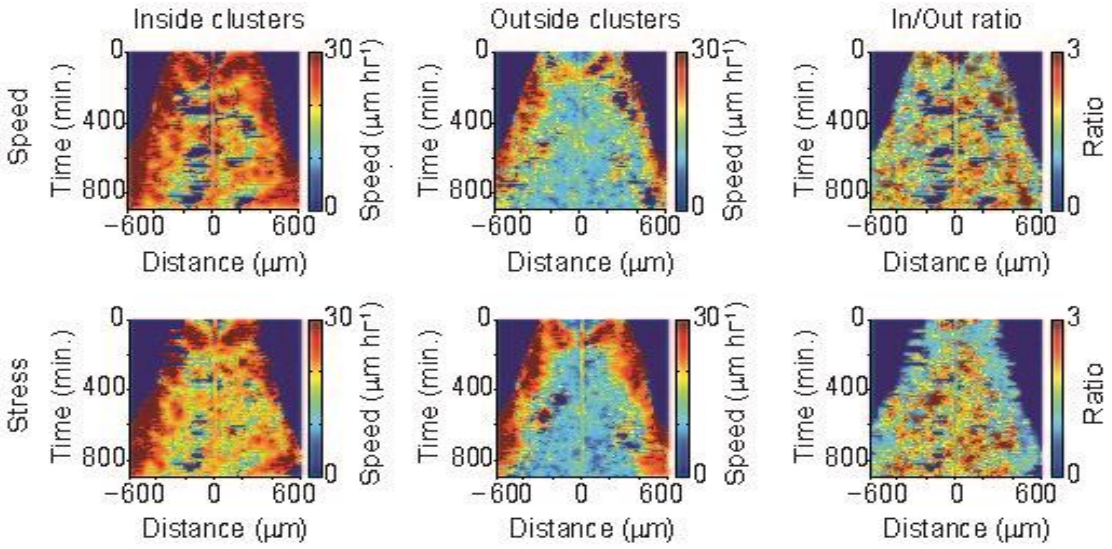

Figure S4: Differential speed inside and outside clusters of coordinated motion (top row) or coordinated stress (bottom row). Average speed of cells inside clusters, outside clusters, and their ratio.

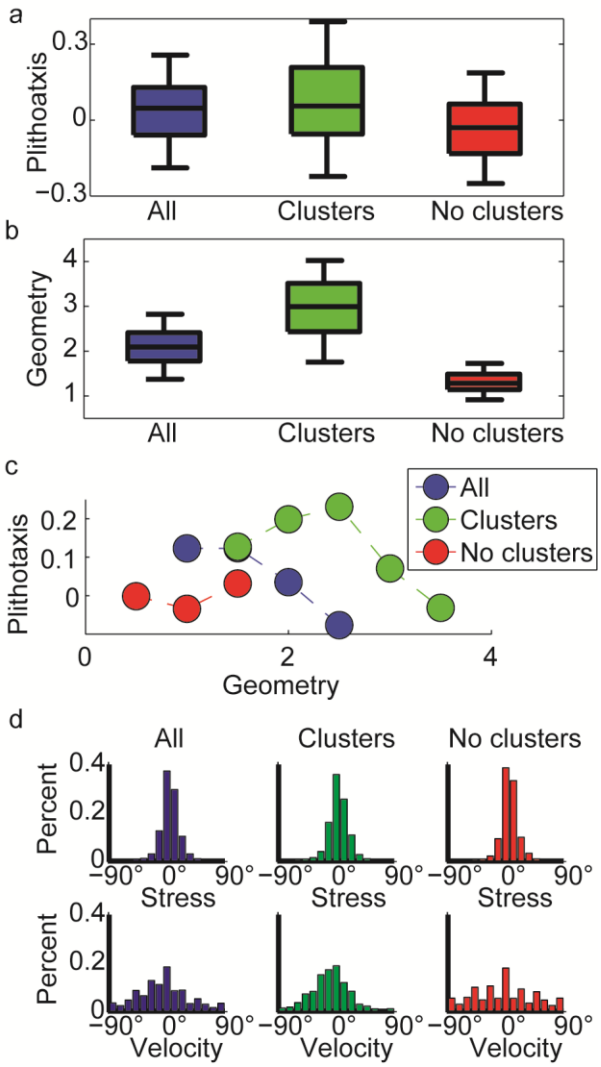

Figure S5: Geometry index is enriched within coordinated motion clusters. (a-b) Distributions of plithotaxis and geometry indices for all ("All") cells, cells that participate in coordinated migrating clusters ("Clusters") and those that do not ("No clusters"). Boxplots were generated from pooled data over time (n = 96). (a) Plithotaxis index is almost non-existent for each category (median all = 0.05, clusters = 0.07, no clusters = -0.02). (b) Geometry index is enriched by a 2.4 fold for cells that participate in clusters (Median: all = 2.1, clusters = 3.02, no clusters = 1.24). (c) Average plithotaxis index as a function of the geometry index. This data shows increased sensitivity to plithotaxis of cells in clusters. (d) Distributions of stress orientation (top) remains similar for all cells, cells within or outside clusters (left to right). Distributions of velocity directions (bottom) revealed the bias toward the direction of the monolayer edge dramatically diminished for cells outside clusters (right).

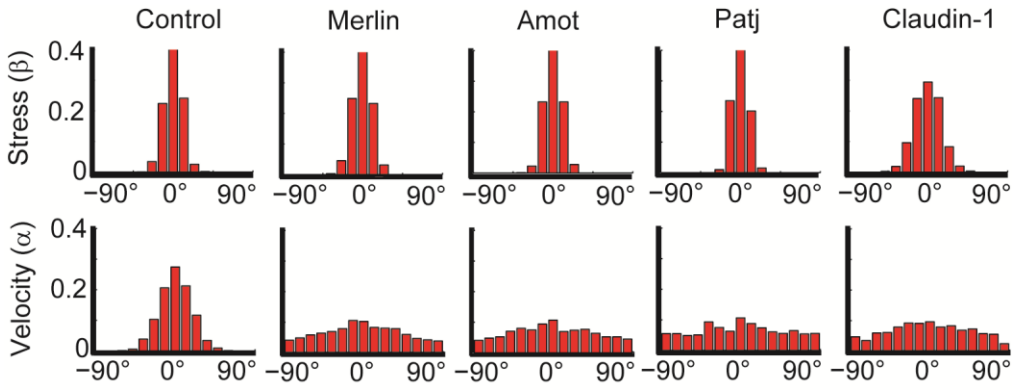

Figure S6: Depletion of the tight-junction proteins Claudin-1, Patj, angiomotin or Merlin dramatically reduced motion-stress alignment by inhibiting the biased direction of velocities while maintaining the bias in the stress orientations. Re-assessment of published MDCK cells wound healing data from (1), number of cells accumulated from three independent experiments: 1539 (control), 1278 (Merlin), 937 (angiomotin), 986 (Patj), 1539 (Claudin-1).

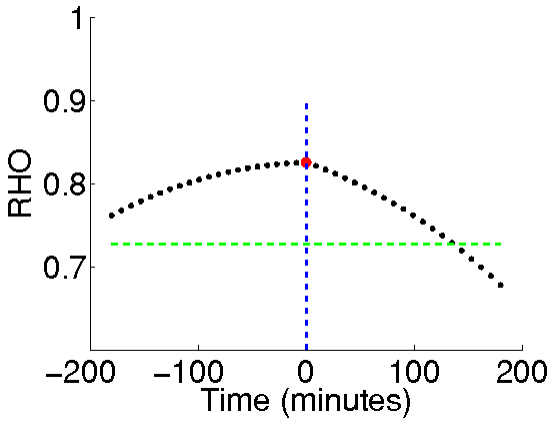

Figure S7: Shear-strain events and flow patterns are temporally synchronized. Cross-correlation analysis between the time-accumulated kymographs of flow probabilities and shear-strain events. Black dots indicate Pearson's cross-correlation between the two kymographs as function of temporal delays. Vertical blue line indicates optimal time lag between shear-strain events and flow patterns. Horizontal green line: Average Pearson's cross-correlation when shear-strain data is scrambled. The experiment corresponds to Fig. 4.

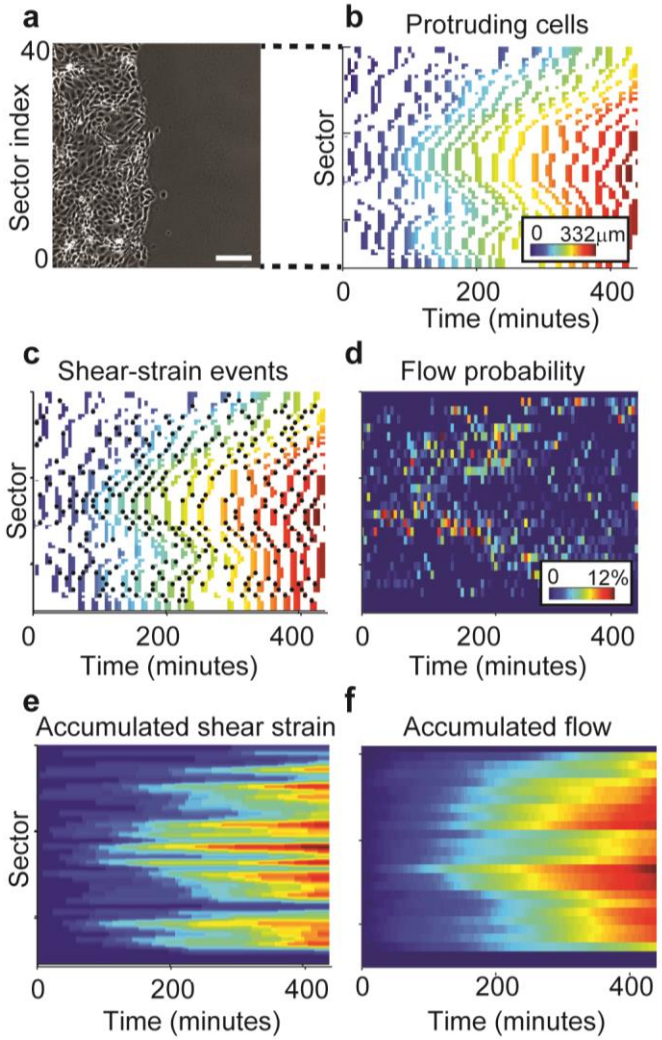

Figure S8: Shear-strain events guide multicellular flow patterns for HBEC wound healing assay. (a) First time frame of a HBEC wound healing assay. The monolayer edge moving along the x-axis is divided into 40 sectors of 15 µm length. Scale bar 100 µm. Supplementary Video S3 shows the entire time-lapse. (b) Protruding cells kymograph. Color encodes the position of the recorded protrusion event along the x-axis. (c) Detection of shear-strain events (black dots) in the protruding cells kymograph. (d) Flow probability kymograph. Color encodes the probability of a tracer to reach the corresponding sector along the monolayer edge. (e) Time-accumulated shear-strain events. (f) Time-accumulated flow probability. Correlation test between accumulated shear-strain events and flow via a permutation test (Methods): $p < 0.002$, Pearson Rho = 0.87, mean scrambled Pearson Rho = 0.62.

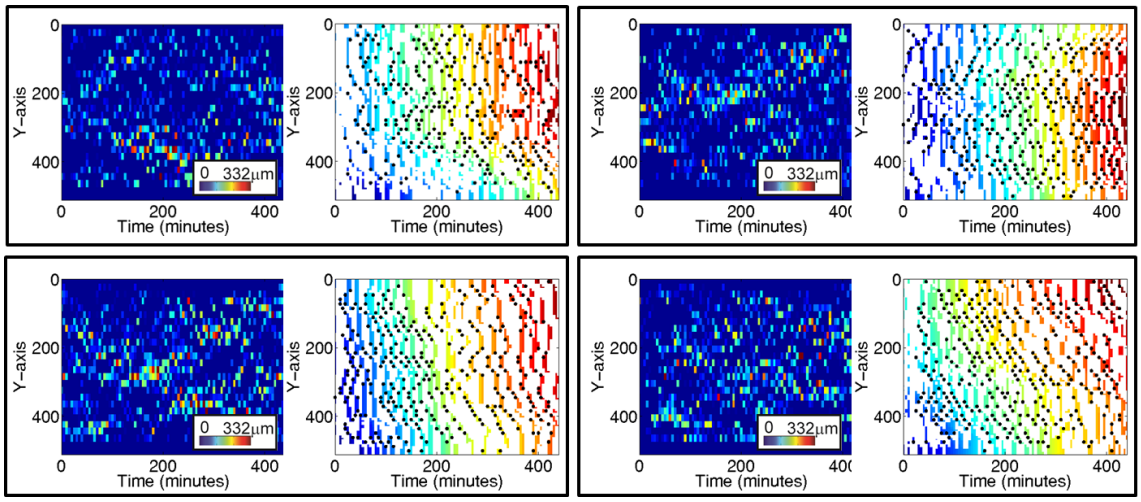

Figure S9: HBEC shear-strain events and corresponding flow probability kymographs. See Fig. 4d and 4g for details.

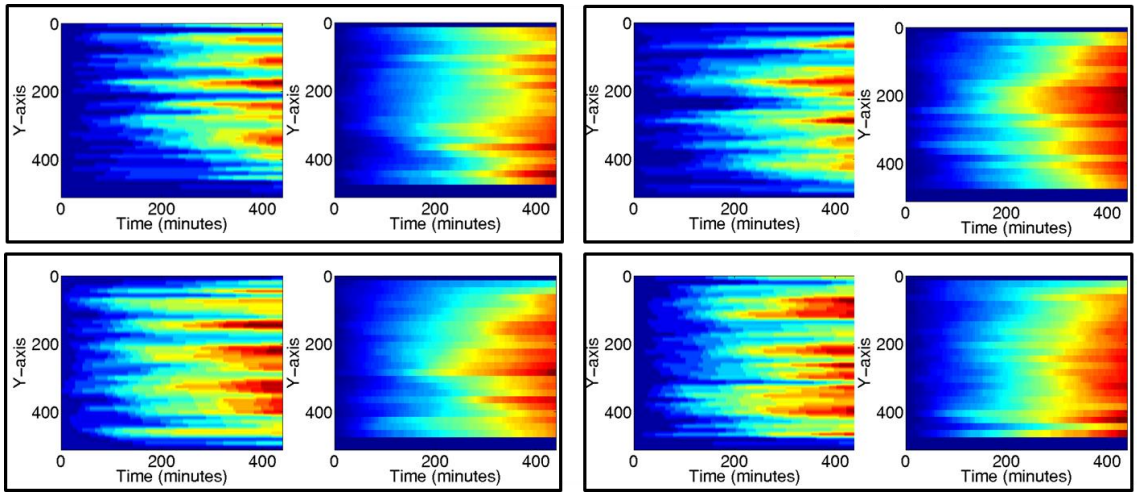

Figure S10: HBEC time-accumulated kymographs of shear-strain events (left) and flow probabilities (right). Four examples (corresponding to the data in Supplementary Fig. S9) are shown to document reproducibility. Permutation test (Methods) gave $p < 0.001$ for all examples to reject the null hypothesis that flow and shear-strain events are spatially independent (unscrambled vs. mean scrambled Pearson Rho: 0.89 vs. 0.66 (top-left), 0.90 vs. 0.65 (top-right), 0.89 vs. 0.63 (bottom-left), 0.92 vs. 0.69 (bottom-right)). See Fig. 4h and 4i for details.

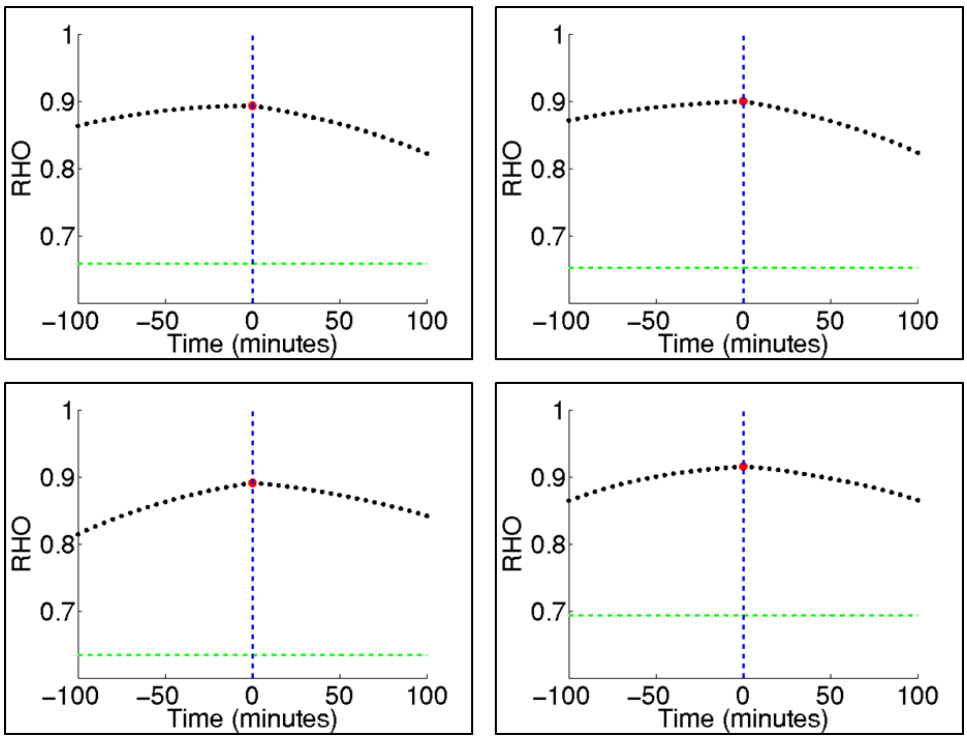

Figure S11: HBEC shear-strain events and flow patterns are temporally synchronized. Cross-correlation analysis between the time-accumulated kymographs of flow probabilities and shear-strain events. Four examples (corresponding to the data in Supplementary Fig. S9) are shown to document reproducibility. Black dots indicate Pearson's cross-correlation between the two kymographs as function of temporal delays. Vertical blue line indicates optimal time lag between shear-strain events and flow patterns. Horizontal green line: Average Pearson's cross-correlation when shear-strain data is scrambled.

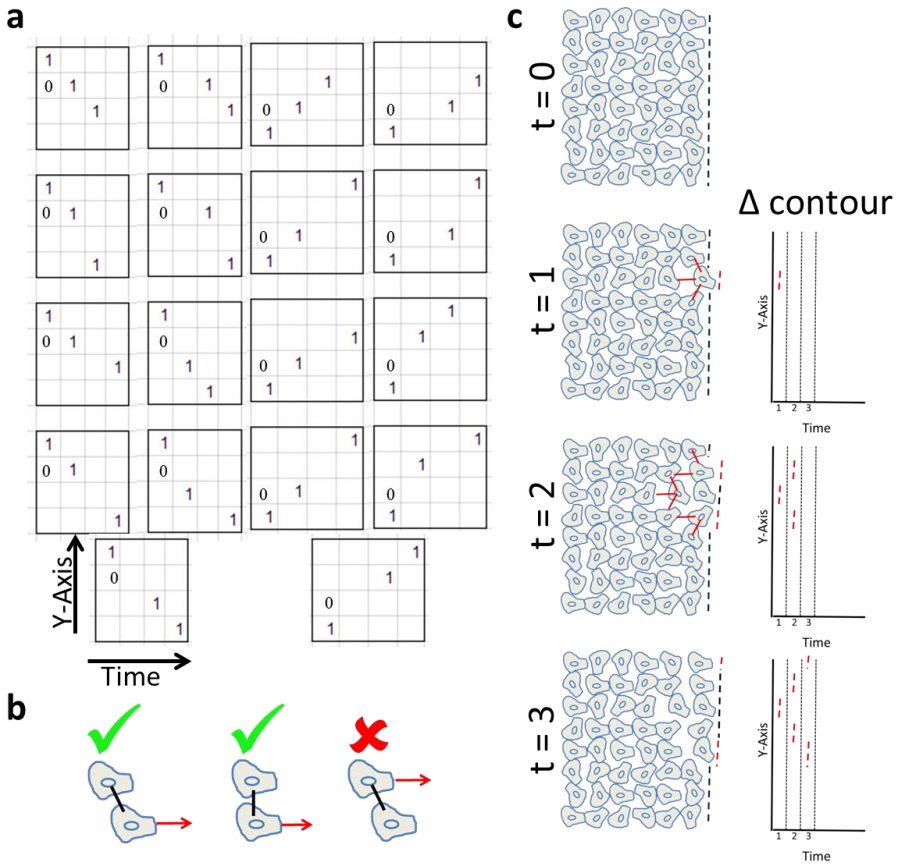

Figure S12: Detection of shear-strain events. (a) 18 spatiotemporal patterns to define shear-strain events in the cell protrusion map by binary template matching. X-axis is time (each bin represents a 5 minute frame), Y-axis is the relative y-coordinate of neighboring protrusion events (each bin represents a 15µm patch). The patterns allow one missing frame and one missing patch along the monolayer edge. The reference point in the pattern is in the top-left or bottom right of the 4-by-4 template and the 0 value in the adjacent patch verifies that one cell will not be responsible for two recorded matched patterns. Shear-strain events fulfilling one of the 18 patterns are recorded. Post processing excludes the 2nd detection of a sector in consecutive time points. (b) Validation that shear-strained neighbors are not located in front of the cell that initiated the shear-strain event (indicated by a red arrow). (c) Schematic of the evolution of a shear-strain event (left, dashed red change in the monolayer front edge) and the corresponding pattern in the cell protrusion kymograph (right). Strain is schematically represented by solid red lines, is hypothesized to guide cells within the monolayer, but is not affecting the cell protrusion kymograph.

Supplementary data S1

Relations between plithotaxis index and the plithotaxis phenomenon: The plithotaxis index is only a lower bound for plithotaxis' contribution to motion-stress alignment, because some of the plithotaxis contribution may be encoded in the geometry index. Accordingly, the geometry index is an upper bound for the contribution of monolayer geometry to motion-stress alignment. Examination of the plithotaxis indices averaged over 0.4-wide bins of geometry index indicates that these bounds are tight: the average plithotaxis index for a geometry index of 0-0.4 is about 0.4 and drops to about 0 for geometry index of 2-2.4 (Supplementary Fig. S13). Under the assumption that the observed motion-stress alignment is explained by the sum of local and global cues, only 0.4 of the plithotaxis can be encoded in the geometry index. Thus, plithotaxis accounts for at most 20% of geometry contribution to motion-stress alignment.

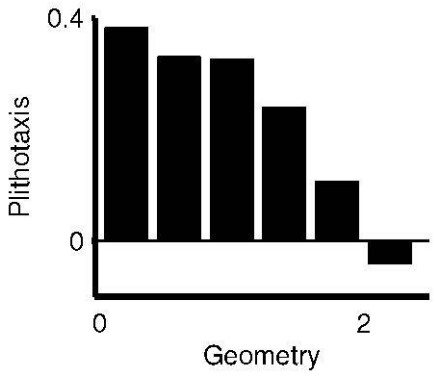

Figure S13: Geometry index and plithotaxis index define tight upper and lower bounds. Average plithotaxis index as function of geometry index from the joint distribution shown in Fig. 1f. Decrease of approximately 0.4 in plithotaxis index is observed over the range of geometry index from 0 to 2.This implies that plithotaxis can account for 20% of the geometry index at most. This rejects the concern that much of the plithotaxis contribution to motion-stress alignment is encoded in geometry index.

Relations between plithotaxis index and *EMD(observed,resampled)*: The plithotaxis index was defined as the difference of the earth movers distance $plithotaxis\_index = EMD(random, observed) - geometry\_index$. This measure was preferred over *EMD(resampled,observed)* because the latter will always give a positive value. Direct comparison of plithotaxis index to *EMD(resampled,observed)* shows that practically (although not theoretically) the absolute value of plithotaxis index is a lower bound to *EMD(resampled, observed)* (Supplementary Fig. S14).

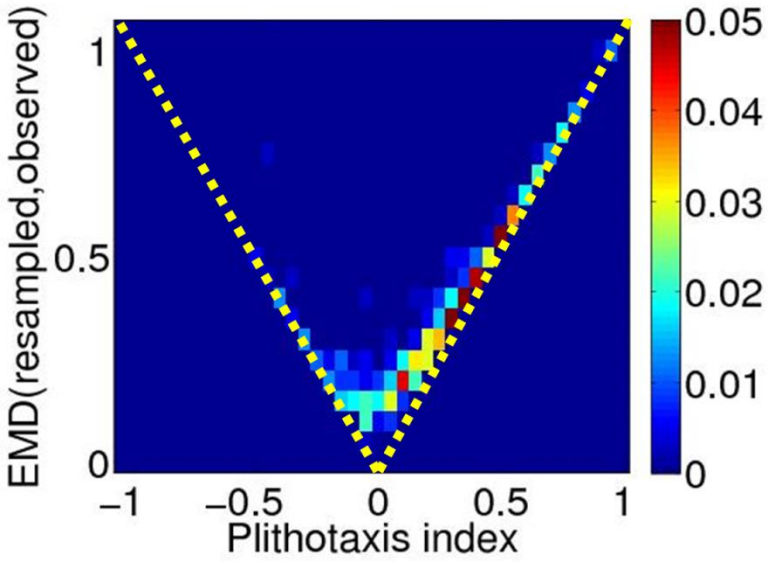

Figure S14: Plithotaxis index versus EMD(resampled,observed). The yellow y = |x| demonstrate that EMD(resampled,observed) ≥ plithotaxis index for this data. The distribution was pulled for all time points (n = 96) in all experiments (N = 4).

Supplementary data S2

Intercellular coordination is not driven by homogeneous accumulation of plithotaxis over space across the monolayer: We assessed whether global organization can be achieved by homogeneous plithotaxis across the monolayer. The hypothesis was that motion-and stress-noise averaging occurs **homogeneously** in groups of adjacent cells. Thus the contribution of plithotaxis could be increased at larger spatial scales. We examined this possibility by averaging velocity and stress over larger spatial bins (with side lengths between 16 um and 160 um), and recalculating the plithotaxis and geometry indices from these bins as "atomic" measurements instead of the original 16μm x 16μm patches. The effect of increasing the spatial averaging area would be to suppress heterogeneities between neighboring regions. Thus, we would expect that a highly localized and heterogeneous phenomenon would be detected less accurately when increasing spatial averaging. In contrast, more homogeneous phenomena will be enhanced. As can be expected, spatial averaging of the inherently globally biased motion and stress led to higher geometry index, with a peak at a patch size of 53um x 53um (approximately 4-9 cells) (Supplementary Fig. S15). No significant increase in plithotaxis index was observed for increasing patch sizes. Thus, the hypothesis of a simple spatially- homogeneous alignment was rejected.

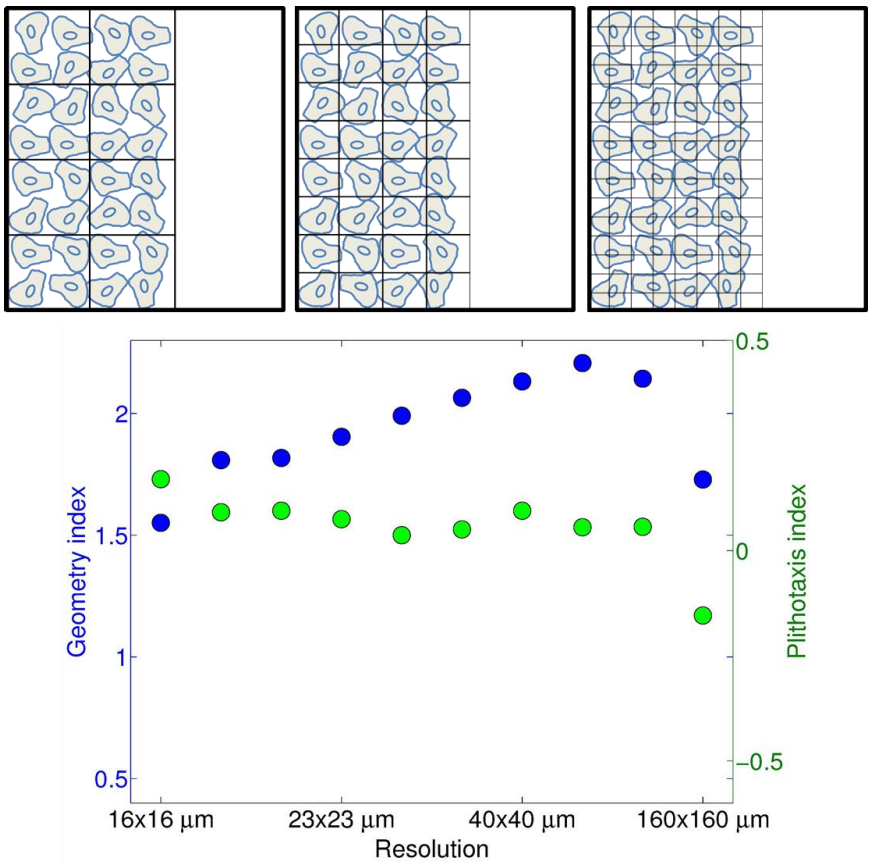

Figure S15: Plithotaxis and geometry indices were calculated at different spatial resolutions (from 16µm x16µm patches to 160µm x160µm patches). (a) A sketch of different resolutions considered. (b) Plithotaxis and geometry indices as a function of spatial resolution. The geometry index (blue) increases monotonically up to patch sizes of 53µm x53µm due to noise averaging of a phenomenon that occurs on a spatial scale of about 50 μm^2. For even larger patch sizes regional motion and stress heterogeneity associated with cluster formation (see Fig. 3) causes a decrease in the geometry index. The plithotaxis index (green) varies much less with the patch size suggesting that plithotaxis is a truly local phenomenon that is localized to a region equal to or smaller than 16 μm^2.

Supplementary videos legends

Video S1: Propagating motion-induced coordination in stress. Time evolution of the probability of a cell to belong to a cluster of coordinated motion (red) or stress (blue), as a function of the distance from the monolayer front edge. Motion-coordination spatially grows in time while the stress clusters propagate to deeper cells. This video corresponds to the experiment displayed in Fig. 3g.

Video S2: Construction of protruding cells kymograph. Left: phase contrast image overlaid by the detected contour. Right: construction of the corresponding protruding cells kymograph. Note the motion waves propagating along the monolayer front edge (left), which are represented by diagonals in the protruding cells kymograph. The video corresponds to the protruding cells kymograph in Supplementary Fig. S8b.

Video S3: Phase contrast imaging of a wound healing experiment using HBECs. The video corresponds to the experiment in Supplementary Fig. S8. The raw data was recorded at 5 minutes per frame, and the replay is at 7 frames per second. The monolayer front migrates at ~35 um/hour.

Supporting references

1. Das, T., K. Safferling, S. Rausch, N. Grabe, H. Boehm, and J. P. Spatz. 2015. A molecular mechanotransduction pathway regulates collective migration of epithelial cells. Nature cell biology 17:276-287.